Research Article

Vol. 26, No. 3 | 5 Feb 2018 | OPTICS EXPRESS 3199

Optics EXPRESS

On-chip calibration and control of optical phased arrays

TIN KOMLJENOVIC* **AND PAOLO PINTUS**

Department of Electrical and Computer Engineering, University of California, Santa Barbara, Santa Barbara, California 93106, USA
tkomljenovic@ece.ucsb.edu

Abstract: Optical phased arrays (OPAs) are important as they allow beam steering and scanning with no moving parts. As their channel count increases, the complexity of control and calibration becomes challenging. We propose an architecture and algorithm that provide rapid on-chip calibration and are scalable to arbitrary channel counts with significantly reduced chip area and reduced overall complexity compared to previously proposed approaches. The optimized phase shifter tuning algorithm – Deterministic Stochastic Gradient Descent (DSGD) - rapidly converges to the optimal state speeding up the digital-to-analog converter based control of large channel count OPAs.

OCIS codes: (010.3640) Lidar; (110.5100) Phased-array imaging systems; (130.3120) Integrated optics devices.

References and links

1. K. Van Acoleyen, W. Bogaerts, J. Jágerská, N. Le Thomas, R. Houdré, and R. Baets, "Off-chip beam steering with a one-dimensional optical phased array on silicon-on-insulator," Opt. Lett. **34**(9), 1477–1479 (2009).
2. J. K. Doylend, M. J. R. Heck, J. T. Bovington, J. D. Peters, L. A. Coldren, and J. E. Bowers, "Two-dimensional free-space beam steering with an optical phased array on silicon-on-insulator," Opt. Express **19**(22), 21595–21604 (2011).
3. K. Van Acoleyen, K. Komorowska, W. Bogaerts, and R. Baets, "One-dimensional off-chip beam steering and shaping using optical phased arrays on silicon-on-insulators," IEEE J. Lightwave Technol. **29**(23), 3500–3505 (2011).
4. J. K. Doylend, M. J. R. Heck, J. T. Bovington, J. D. Peters, M. L. Davenport, L. A. Coldren, and J. E. Bowers, "Hybrid III/V silicon photonic source with integrated 1D free-space beam steering," Opt. Lett. **37**(20), 4257–4259 (2012).
5. D. Kwong, A. Hosseini, J. Covey, Y. Zhang, X. Xu, H. Subbaraman, and R. T. Chen, "On-chip silicon optical phased array for two-dimensional beam steering," Opt. Lett. **39**(4), 941–944 (2014).
6. A. Yaacobi, J. Sun, M. Moresco, G. Leake, D. Coolbaugh, and M. R. Watts, "Integrated phased array for wide-angle beam steering," Opt. Lett. **39**(15), 4575–4578 (2014).
7. J. C. Hulme, J. K. Doylend, M. J. R. Heck, J. D. Peters, M. L. Davenport, J. T. Bovington, L. A. Coldren, and J. E. Bowers, "Fully integrated hybrid silicon two dimensional beam scanner," Opt. Express **23**(5), 5861–5874 (2015).
8. H. Abediasl and H. Hashemi, "Monolithic optical phased-array transceiver in a standard SOI CMOS process," Opt. Express **23**(5), 6509–6519 (2015).
9. F. Aflatouni, B. Abiri, A. Rekhi, and A. Hajimiri, "Nanophotonic projection system," Opt. Express **23**(16), 21012–21022 (2015).
10. H. Nikkhah, K. Van Acoleyen, and R. Baets, "Beam steering for wireless optical links based on an optical phased array in silicon," Ann. Telecommun. **68**(1–2), 57–62 (2013).
11. J. Sun, E. Hosseini, A. Yaacobi, D. B. Cole, G. Leake, D. Coolbaugh, and M. R. Watts, "Two-dimensional apodized silicon photonic phased arrays," Opt. Lett. **39**(2), 367–370 (2014).
12. J. Sun, E. Timurdogan, A. Yaacobi, E. S. Hosseini, and M. R. Watts, "Large-scale nanophotonic phased array," Nature **493**(7431), 195–199 (2013).
13. J. Sun, E. Timurdogan, A. Yaacobi, Z. Su, E. S. Hosseini, D. B. Cole, and M. R. Watts, "Large-scale silicon photonic circuits for optical phased arrays," IEEE J. Sel. Top. Quantum Electron. **20**(4), 8201115 (2014).
14. K. Van Acoleyen, H. Rogier, and R. Baets, "Two-dimensional optical phased array antenna on silicon-on-insulator," Opt. Express **18**(13), 13655–13660 (2010).
15. W. Guo, P. R. A. Binetti, C. Althouse, M. L. Masanovic, H. P. M. M. Ambrosius, L. A. Johansson, and L. A. Coldren, "Two-Dimensional Optical Beam Steering With InP-Based Photonic Integrated Circuits," IEEE J. Sel. Top. Quantum Electron. **19**(4), 6100212 (2013).
16. K. Sayyah, O. Efimov, P. Patterson, J. Schaffner, C. White, J.-F. Seurin, G. Xu, and A. Miglo, "Two-dimensional pseudo-random optical phased array based on tandem optical injection locking of vertical cavity surface emitting lasers," Opt. Express **23**(15), 19405–19416 (2015).

#309169 https://doi.org/10.1364/OE.26.003199
Journal © 2018 Received 16 Oct 2017; revised 28 Dec 2017; accepted 26 Jan 2018; published 30 Jan 2018

17. D. Kwong, A. Hosseini, Y. Zhang, and R. T. Chen, "1× 12 unequally spaced waveguide array for actively tuned optical phased array on a silicon nanomembrane," Appl. Phys. Lett. **99**(5), 051104 (2011).
18. J. K. Doylend, M. J. R. Heck, J. T. Bovington, J. D. Peters, and J. E. Bowers, "Free-space beam steering using silicon waveguide surface gratings," in IEEE Photonic Society 24th Annual Meeting, Arlington, VA (2011), pp. 547–548.
19. D. N. Hutchison, J. Sun, J. K. Doylend, R. Kumar, J. Heck, W. Kim, C. T. Phare, A. Feshali, and H. Rong, "High-resolution aliasing-free optical beam steering," Optica **3**(8), 887–890 (2016).
20. C. V. Poulton, M. J. Byrd, M. Raval, Z. Su, N. Li, E. Timurdogan, D. Coolbaugh, D. Vermeulen, and M. R. Watts, "Large-scale silicon nitride nanophotonic phased arrays at infrared and visible wavelengths," Opt. Lett. **42**(1), 21–24 (2017).
21. C. V. Poulton, A. Yaacobi, D. B. Cole, M. J. Byrd, M. Raval, D. Vermeulen, and M. R. Watts, "Coherent solid-state LIDAR with silicon photonic optical phased arrays," Opt. Lett. **42**(20), 4091–4094 (2017).
22. T. Komljenovic, R. Helkey, L. Coldren, and J. E. Bowers, "Sparse aperiodic arrays for optical beam forming and LIDAR," Opt. Express **25**(3), 2511–2528 (2017).
23. M. A. Vorontsov, G. W. Carhart, and J. C. Ricklin, "Adaptive phase-distortion correction based on parallel gradient-descent optimization," Opt. Lett. **22**(12), 907–909 (1997).
24. J. Kennedy and R. Eberhart, "Particle swarm optimization," in Proceedings of IEEE International Conference on Neural Networks IV (1995), pp. 1942–1948.
25. L. B. Soldano and E. C. M. Pennings, "Optical multi-mode interference devices based on self-imaging: principles and applications," J. Lightwave Technol. **13**(4), 615–627 (1995).
26. M. Bachmann, P. A. Besse, and H. Melchior, "General self-imaging properties in N × N multimode interference couplers including phase relations," Appl. Opt. **33**(18), 3905–3911 (1994).

1. Introduction

Chip-scale optical phased arrays (OPA) are of interest, primarily due to a need for a low-cost light detection and ranging (LIDAR) system for autonomous driving where it is believed that such a system, enabled by the scale of semiconductor manufacturing, would be a game changer. There are many other applications that would benefit from high-performance OPAs such as free space communications, holographic displays and biomedical imaging. Mechanical steering is common, but an OPA offers many advantages such as reduced size and weight as well as increased speed due to lack of inertia.

Great progress has been made in recent years with a focus on integrated phased arrays [1–21] and many impressive demonstrations. In this manuscript we study an integrated OPA where phase control is used to steer only in one of the axis, while the other axis is steered by wavelength such as in [7,19]. Such approach has a distinct advantage compared to a purely phase steered 2D array due to the significant reduction in the number of controls required. A 1D OPAs need only $N + 1$ controls (N phases and 1 wavelength) compared to NxM controls needed for 2D phase array. Practical demonstrations of such arrays had generally limited channel counts (128 [19]) if the OPAs have included steering elements (phase shifters). More complex OPAs without phase shifters comprising up to 1024 elements have been demonstrated [20], but they obviously lack the steering capability. Furthermore, in many cases, external cameras were used to calibrate the arrays with limited side-mode suppression ratios (SMSR) despite using various alignment strategies such as hill-climbing or gradient descent algorithm [7,19]. Calibration and alignment not only is time consuming, but also has problems such as temperature changes and aging of the components. The temperature changes can be compensated to a certain extent with look-up tables, but at the expense of slowing down the calibration process further, while there is no clear way to address aging in e.g. phase shifters. Some applications require OPAs with thousands or more channels, such as imaging at 1 km or more or free space optical communications over thousands of km. If such OPAs are to be moved from the laboratory stage, control and calibration has to be simplified and made robust to external influences and aging. In this work, we propose both the architecture and an algorithm that combined allow for fast on-chip calibration and control.

The manuscript is organized as follows. In Section II we introduce a modified control algorithm for OPAs that speeds up the convergence compared to other popular algorithms even at larger channel counts. In Section III we introduce the on-chip calibration and control sub-system that can scale to practically arbitrary channel counts and takes advantage of the algorithm introduced in Section II. Finally we give a brief discussion on the proposed method and give conclusions in Section IV.

2. OPA control algorithm

We study an OPA as shown in Fig. 1, where the input signal is split via a star coupler to N phase shifters and ultimately N emitter gratings. In our preferred embodiment, the OPA uses a star coupler for power splitting as it offers high fan-out count, small pitch, multiple wavelengths operation, low insertion loss and power profile shaping for reducing the sidelobes. As an alternative, a multimode interference (MMI) coupler tree could be used with potentially the biggest advantage compared to a star coupler structure being the uniform phase delay. An MMI tree generally can have low loss, but the loss tends to increase as the width of the MMIs is reduced (e.g [20].) – which is necessary for a small pitch emitter. It also provides uniform power distribution, which can in some circumstances be a disadvantage resulting with increased sidelobes. We would also like to point out that, despite having uniform phase delay in the splitter region, the MMI tree OPA still probably requires calibration in a potential full LIDAR system as there are many other sources of phase errors such as thermal gradients and process non-uniformity for both the passive and active (phase shifters) components, especially as chip sizes continue to increase.

In our analysis, we study a 512 channel OPA, set the grating pitch to be 1.25 µm and set the operating wavelength to be $\lambda = 1.55$ µm. This allows steering the main lobe to around ± 13.9° until a grating lobe appears in the visible space and, with the proper design of the elementary emitter, much wider steering by using the directivity of the elementary emitter to suppress the grating lobes. For simplicity we use an omnidirectional elementary emitter in our calculations. Further reduction of the pitch would improve the grating lobe performance, but the optical crosstalk can become a problem. We ignore the crosstalk in our analysis, but point out that both the algorithm and the architecture we describe below can be used with larger pitch OPAs that have multiple grating sidelobes. Sidelobes in that case can be suppressed with sparse aperiodic arrays as analyzed in [23], but with a penalty of reduced power in the main beam.

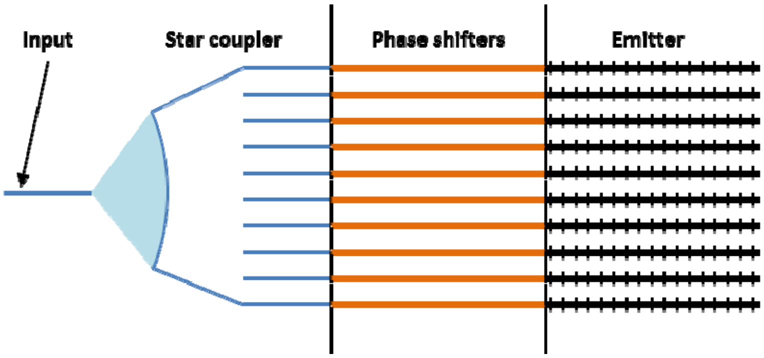

Fig. 1. Optical phase array (OPA) as studied comprises of a star coupler (splitting the input into N waveguides), N phase shifters and N emitters.

The optimization of an OPA is a challenging task due to explosion in complexity as the number of channels is increased. The emitters in a typical OPA will most likely be controlled by a corresponding number of digital-to-analog converters (DAC). The number of bits in a DAC is an optimization parameter, and depending on the required OPA performance, lower number of bits (6-8) might be satisfactory. The total number of states is given by:

$$\text{No. states} = 2^{N \cdot B} \tag{1}$$

where N is the number of waveguides or emitters and B is the number of bits in DACs. In our study, we implement the control with 16-bit DACs, as a harder problem to solve and to better illustrate the superiority of our novel algorithm. This results with a solution space for the $N = 512$ channel OPA with number of states much larger than the number of atoms in the universe, currently estimated at between 10^{72} and 10^{82}.

In the study of the sparse aperiodic arrays [22], where the positions of the emitters were optimized for the best performance, the fitness function was given by the directivity in the target direction plus the achieved SMSR. Such, more complicated, fitness function was necessary to optimize the array element placement for the best performance in given direction. We note that once the arbitrary array elements locations are set, we can use a simpler fitness function such as the power in the target direction. The change of fitness function greatly simplifies the solution space and allows us to improve the optimum search algorithm as well.

To show the benefit of this novel approach let us consider a simpler case of a 32-channel OPA with 6-bit DACs. Both the channel count and the number of bits are decreased in order to make the images more illustrative. In Fig. 2, a subspace of the fitness solution space is shown, where the value of channel 15 and 16 are swept while the remaining channels are kept constant. Those plots are a projection of the solution in a 2-dimensional sub-space, while the full solution space is N dimensional. On the left-hand side of Fig. 2, the fitness function combines the directivity in the main lobe direction $D(\alpha)$ with the SMSR ratio, while on the right-hand side, the fitness function is the power in the main lobe encompassed in twice the diffraction limited 3 dB beam-width $P(\alpha)$. In all plots, the sign of the fitness function is switched, so the minimum corresponds to higher fitness value.

To demonstrate the advantage of the new fitness function, we consider two different channel-configurations. In the first case, which is shown on the top of Fig. 2, all channels (i.e., from 1 to 14 and from 17 to 32) are set at the optimal value while the value of channel 15 and 16 are swept in the sub-space. Vice versa, on the bottom of Fig. 2, we assume that all the remaining channel have a random value.

In the former working condition, both fitness function show a smooth shape. On the other hand, when all the remaining channel are randomized, only the power-based fitness function shows a clear minimum in the 2D-subspace, while $D(\alpha) + SMSR$ has an irregular behavior. As proved by this illustrative example, the solution space is much simpler if $P(\alpha)$ is used as fitness function, which simplifies the work of the optimizer and allows for independent channel pre-alignment. Depending on system constraints, both fitness functions do not necessarily converge to identical solutions, but they lead to maximization of power in the main lobe and can be used to steer the beam. Suitability of simplified fitness function for OPA control is demonstrated in Fig. 6 where beam is rapidly steered in number of directions.

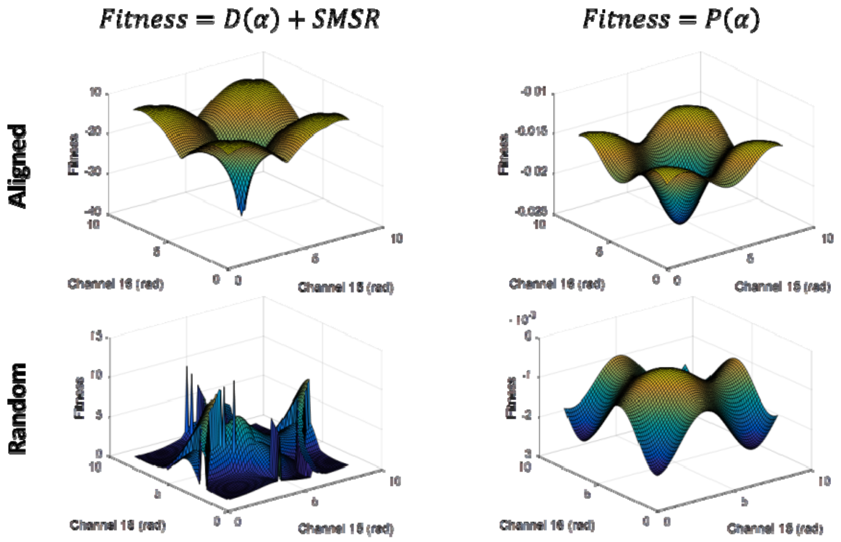

Fig. 2. Fitness solution space for 32-channel OPA using 6-bit DACs as two channels are swept (channel 15 and 16) for two different fitness functions and aligned or randomized phases of the remaining channels. See text for details.

We compare three optimization algorithms using the simplified fitness function based on $P(\alpha)$. We utilize one of the most popular global search optimizations – particle swarm optimization (PSO) [24] and a popular adaptive wavefront control technique based on stochastic parallel gradient descent (SPGD) [23]. For details on the PSO algorithm, reader is referred to the literature while we will briefly describe the SPGD as it is partly reused in our proposed algorithm. In a SPGD algorithm with N control channels, it is assumed that it is possible to calculate the fitness function as $\mathrm{F} = \mathrm{F}(u_1, u_2, \ldots, u_\mathrm{N})$. Small random perturbations δu_j are applied to every channel simultaneously. Said random perturbations have fixed amplitudes $|\delta u_\mathrm{j}| = \delta u$ with random signs with equal probabilities for $\delta u_\mathrm{j} = + \delta u$ and $\delta u_\mathrm{j} = -\delta u$. Fitness perturbation is defined as $\delta\mathrm{F} = \mathrm{F}(u_1 + \delta u_1, u_2 + \delta u_2, \ldots, u_\mathrm{N} + \delta u_\mathrm{N})\text{-}\mathrm{F}(u_1, u_2, \ldots, u_\mathrm{N})$ and the stochastic approximation to the true gradient component $\partial\mathrm{F}/\partial u_\mathrm{j}$ by the ratio $\delta\mathrm{F}/\delta u_\mathrm{j}$. Now we can apply conventional gradient procedures, with the only difference being that instead of the true gradient, the stochastic approximation is used. The benefit is that stochastic gradient approximation is a single calculation step regardless of the number of dimensions of the system. For more details see reference [23].

We note that both algorithms are relatively slow in converging to the optimal solution, which motivated us to develop a novel algorithm that improves on the stochastic parallel gradient descent by introducing an initial deterministic part to pre-align the phase shifters closer to the optimal locations and then let the stochastic gradient provide fine tuning to the optimal solution. We call the new algorithm deterministic-stochastic gradient descent (DSGD). The pseudo-code for the deterministic part of the algorithm is given below in Fig. 3, while in the stochastic part, we use identical code as in [23] with the addition of reducing the step size (δu) as the optimization progresses. The deterministic part is made possible with the use of simplified fitness function as each emitter is tuned to provide maximum power in the direction where the OPA is pointed to. It is possible to fully align each phase shifter using the deterministic part of the algorithm, but that would lead to an excessive number of evaluations (large number of DAC states with 8- or 16-bit DACs) so the optimization algorithm is broken into two parts. In the first part, the number of DAC steps is reduced to a smaller subset of values (typically 4-16 steps) which is a relatively fast way to pre-tune the array. By coarsely pre-tuning the emitters, we greatly simplify the problem for the stochastic part, which starts closer to the optimal solution and avoids being stuck in local minima. SPGD then fine tunes the OPA to provide majority of power in the main lobe.

A direct comparison in the convergence of the algorithms is shown in Fig. 4. The DSGS is more than an order of magnitude faster than the PSO algorithm and the speed difference increases as the fitness is improved. The SPGD works reasonably well in the initial stages of the optimization, outperforming the PSO, but due to limited randomness and the complexity of the problem makes slow progress in later stages, often being stuck in a local minimum. The PSO, owning to its ability to escape local minimums, converges to a good result but with very large number of evaluations. For the DSGS we initially optimized two most significant bits using deterministic approach (2,048 evaluations) and then move to SPDG using 1,000 evaluations for each of the 5 step sizes where the steps were equal to 2^6, 2^5, 2^4, 2^3 and 2^2 (5,000 evaluations), bringing the total number of evaluations to 7,048 evaluations. For the pure SPDG we used 10,000 evaluations for each of the 8 step sizes used (80,001 evaluations total), while for the PSO we have utilized the build-in Matlab routine with 200 swarm elements and let it run for 3 hours on an i7 quad-core CPU reaching 207,600 evaluations. In all cases the initial phases are fully randomized, corresponding to a worst case scenario.

We plot the optimized far-field patterns and corresponding phases of the individual phase shifters in Fig. 5, and also summarize key parameters of the synthesized beams in Table 1. It is clear that the proposed DSGD algorithm is superior for considered type of problems.

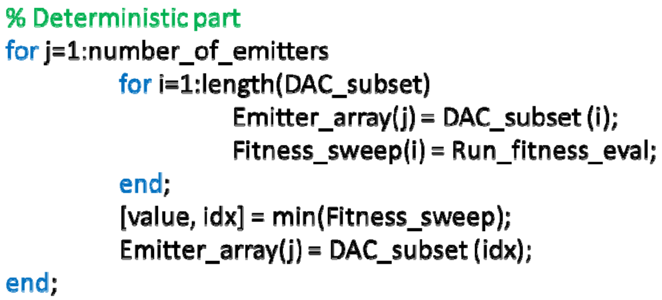

```
% Deterministic part
for j=1:number_of_emitters
        for i=1:length(DAC_subset)
                Emitter_array(j) = DAC_subset (i);
                Fitness_sweep(i) = Run_fitness_eval;
        end;
        [value, idx] = min(Fitness_sweep);
        Emitter_array(j) = DAC_subset (idx);
end;
```

Fig. 3. Pseudo-code for the deterministic part of the DSGD algorithm. The reduced set of DAC points (DAC_subset) is usually 2-4 most significant bits of the DAC resulting with 4-16 evaluations for channel before proceeding with stochastic algorithm. DAC_subset ⊂ DAC_states, where DAC_states is the full DAC range. Emitter_array are controls of individual emitters arranged as an array; one can think of it as an array that stores DAC states or voltages for pointing the beam at a certain direction and is the array that is being optimized.

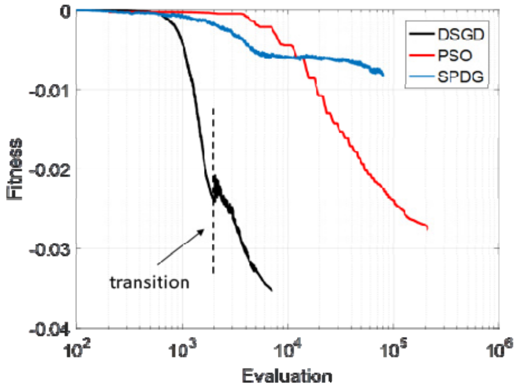

Fig. 4. Convergence of the three considered algorithms. Note that the *x*-axis is plotted using a logarithmic scale. For the DSGD, we show the point in which the algorithm transitions from deterministic to stochastic part.

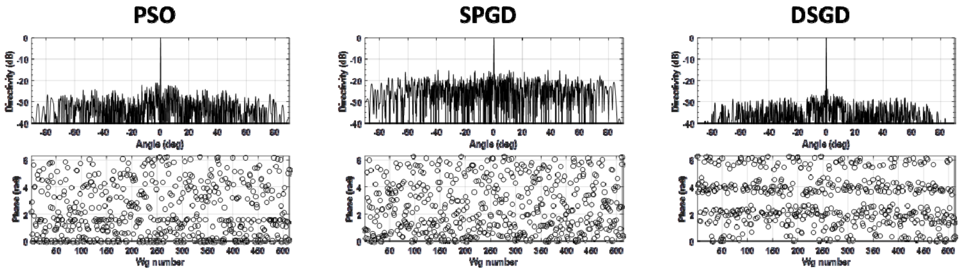

Fig. 5. Comparison between final results for the three studied algorithms. The top row shows the far-field patterns, while the bottom row shows the phases on the individual phase shifters. Some key parameters are summarized in Table 1.

Table 1. Comparison between the algorithms used to control the OPA

	PSO	SPGD	DSGD
SMSR:	21.12	15.11	24.07
Power in main beam:	0.58	0.22	0.76
Evaluations required:	207,600	80,001	7,048

We finally optimize the beam using the DSGD algorithm in various directions, even when the grating lobe of the same magnitude appears, as we use an omnidirectional elementary emitter in the simulations. The algorithm can reach a similar level of performance, regardless of the direction angle, in comparable time of only around 7,000 evaluations as shown in Fig. 6. We used identical DSGD settings as before.

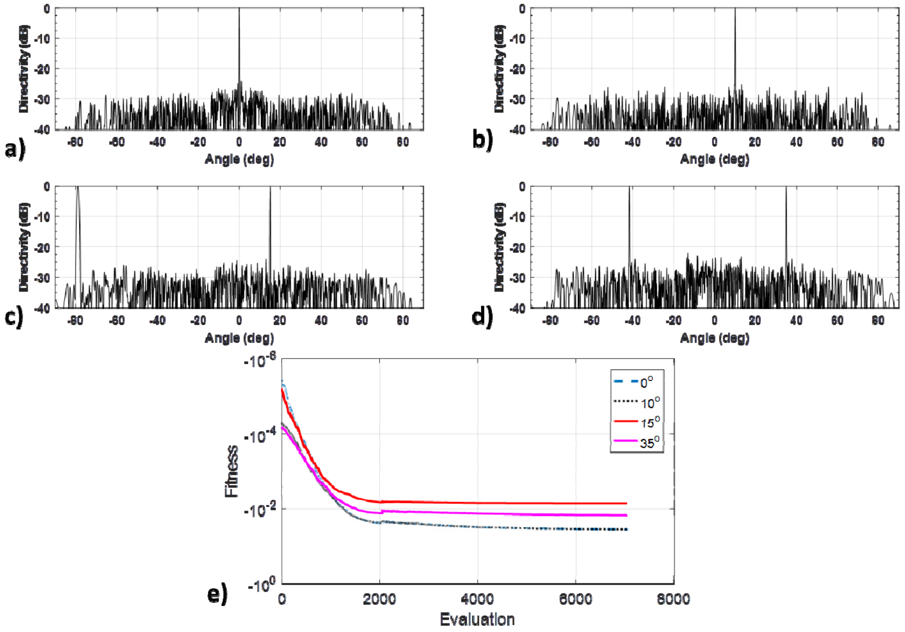

Fig. 6. Synthesized far-field patterns at (a) 0° (b) 10° (c) 15° and (d) 35°. The convergence of the fitness function is shown in (e). The speed of convergence is very similar between different steering angles, but it is interesting to see that they converge to a different value. The reason is the grating lobe that reduces the power in the main lobe once it is steered past ~13.9°. The initial fitness also varies, but that is dependent on the initial randomization of the phases.

The optimizations so far mimic the optimization that would be performed if an external camera was used. As we only use the power in the main beam (target angle) for optimization, neglecting the power/data outside the region of interest, it is possible to zone the readout of the camera to only few pixels and increase the readout rate resulting in faster beam formation. The increased speed is a welcome improvement, but still the system requires external components for calibration and is susceptible to external influences and aging. It turns out we can do much better by including added functionality to the OPAs to provide on-chip calibration and control as we show in the next section.

3. On-chip control subsystem

There have been ideas to include an on-chip monitor to an OPA system such as e.g. GRIN lens with a photodetector array [7]. Such a system is relatively complex and, according to the design shown in [7], it occupies a large area compared to the emitting array. Finally no details on control were given. An approach using MMI couplers was demonstrated for 8-channel OPA in [15]. Here the authors employed an MMI tree that for *N* channel array comprises of *N* 1x3 MMIs, (*N* + 1) modified 2x1 MMIs and (*N*-1) photodetectors. The authors have demonstrated on-chip calibration and control, but it is obvious that such an approach has poor scaling for OPAs with larger channel counts. An added complication was the difference in the OPA phase and the phase at the reference plane where the on-chip control was implemented due to relatively long waveguides with bends used to route the signals on the chip.

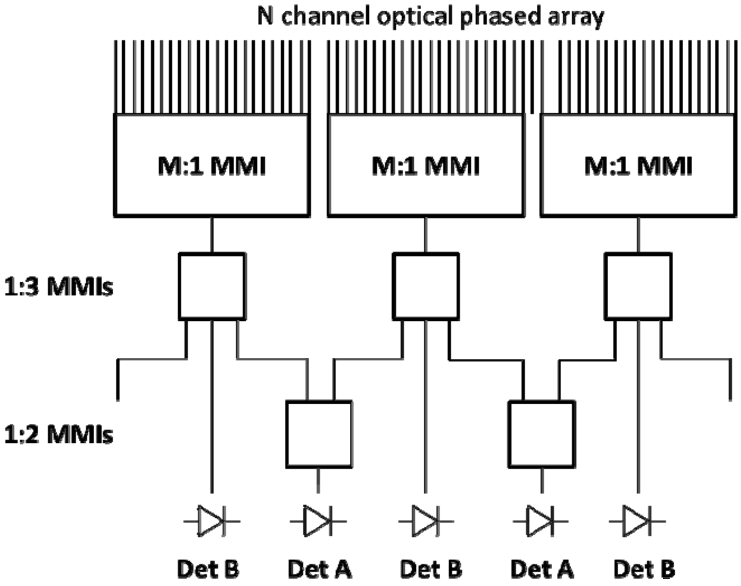

Fig. 7. Proposed on-chip calibration and control of high-channel count OPAs. Larger number of waveguides are coupled to M:1 MMI whose output is coupled through 1:3 MMIs directly to detectors B or through a 1:2 MMI to a detectors A. Details of the operation are in the text.

We propose an alternative configuration that has much better scaling to larger channel counts with fewer elements as shown in Fig. 7. The on-chip control comprises of a M:1 MMIs that we describe in more detail later on. Its output is split in 1:3 MMIs to detectors of type B or is routed through 2:1 MMIs to detectors of type A. Both detectors can be the same type of device, and the distinction is only in the role they play during the alignment. In case the channel count is smaller, only a single M:1 MMI and one detector can be used for the control, while with the increase in the total number of channels, it is advisable to split the control in multiple sets of *M* waveguides. The exact number of waveguides connected to each M:1 MMI is an optimization parameter. Each M:1 MMI and the corresponding type B detector is used to align *M* waveguides as will be described with the help of Figs. 8 and 9, while type A detectors are used to align the phases of channels corresponding to neighboring M:1 MMIs similarly to the alignment of neighboring channels in [15]. There might be some channels between the M:1 MMIs that are not coupled, depending on the pitch in the optical phased array and the required spacing between the MMIs. In most scenarios, with the use of a high-contrast waveguide platform like Si-SiO$_2$, that spacing can be very small leading to potentially one channel without direct control. For that channel the control can be extrapolated from neighboring channels.

Similarly to the optimization described in Section II where we optimized the power at single location, here we maximize the received power in detector B for each set of *M* channels. When the power at the detector is maximized, we know that the input phases are set to values that correspond to the maximum power being imaged at the single port of the M:1 MMI. Those phases can be calculated analytically or simulated numerically and used to compute the phases in the individual waveguides. Furthermore, by tuning a single phase shifter, its efficiency can be determined from the periodicity in the photodetector signal. But before we show simulation results for M:1 MMI, we first establish size scaling of M:1 MMIs, which will show the important benefit of the proposed approach in terms of on-chip size.

As the MMI is a reciprocal component, we study the inverse problem that is somewhat simpler. We excite the central port at one side and simulate the evolution of electrical field as it propagates. The general behavior of MMIs is well known [25, 26], but it might not be that obvious that the larger number of imaged peaks appear the shorter the MMI is. As in our case we want to have a M:1 MMI coupler, where *M* is a large number, this directly leads to very short structures. In the case simulated in Fig. 8 for 30 μm wide MMI excited by 2 μm wide waveguide there are 12 resolvable peaks at the distance of 158 μm resulting with ability to control 2.5 μm pitch OPA. Furthermore the inputs to the MMI are straight waveguides coming from the OPA removing the problems associated with difference in measured and OPA reference frames outlined in [15]. By shortening the length, smaller pitches can also be controlled although with some reduction in coupled energy as peaks are less and less pronounced.

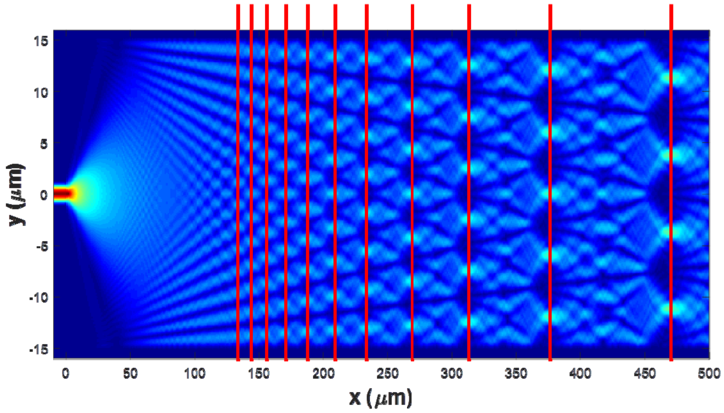

Peaks	Pitch (μm)	Length (μm)
4	7.50	472
5	6.00	376
6	5.00	313
7	4.29	270
8	3.75	234
9	3.33	208
10	3.00	187
11	2.73	170
12	2.50	158
13	2.31	144
14	2.14	134

Fig. 8. Imaging properties of a 30 μm wide. The number of images increases at shorter lengths which is the optimal behavior for the M:1 MMI as envisioned in Fig. 8. The table on the right shows the number of peaks and pitch at given length corresponding to the vertical red lines that serve as a guide to the eye. All dimensions are in μm.

As the OPA that we studied in Section II had 1.25 μm pitch, we now design an MMI suitable for control of said OPA. We set the width of the MMI region to 50 μm, which will correspond to 40 channels at 1.25 μm pitch. With the optimization of the length, we show that control of such OPA is indeed possible with ~89% power coupled as shown in Fig. 9. The total length of the MMI is only 127 μm, excluding the tapers that are an optimization parameter, allowing on-chip control with significant reduction in the on-chip area. There is a large phase variation between the channels (Fig. 9(c)), but this can easily be corrected with control electronics such as microcontroller or FPGA by using the scattering matrix of the MMI as will be described later in the calibration and control part. In some cases, initial calibration of the MMI scattering matrix can be made on a separate test structure from the same wafer run; or initial pre-alignment to determine exact phase shifts can be performed using external instrumentation. Necessity of such steps depends on the quality of fabrication process, which only tends to increase as more advanced fabrication nodes are used for photonic integrated circuits.

The scaling is also very favorable in terms of other components. Obviously, the biggest tradeoff is in the number of channels in the M:1 MMI. For a given N channel OPA, the on-chip control needs (N/M) M:1 MMIs, (N/M) 1:3 MMIs, (N/M-1) 2:1 MMIs and (N/M + 1) photodetectors. It is clear that with large M of 50 or even 100, the component count is significantly reduced. Furthermore, the alignment algorithm outlined in Section II can be performed in parallel for each M waveguide coupled to a single M:1 MMI, further reducing the time required for alignment. With modulator and photodetector bandwidths in GHz ranges, the calibration could be performed almost instantly, since the proposed algorithm converges in less than 10,000 evaluations for 512 channel count.

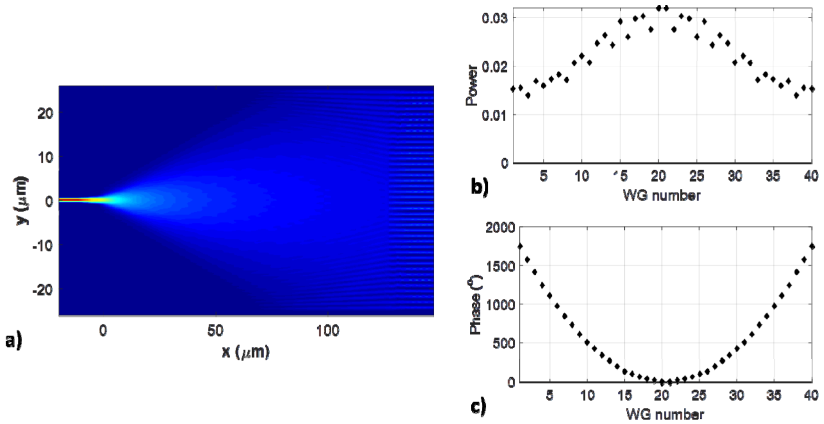

Fig. 9. (a) M:1 MMI for control of 1.25 µm pitch OPA. There are in total 40 waveguides in 50 µm wide MMI. (b) Around ~89% of power can be coupled by using tapers at the input and output. (c) The variation in absolute phase between waveguides increases for shorter MMIs (smaller pitch), but is something that is straightforward to include in the control electronics.

Combining the benefit of the alignment algorithm, previously described, with the on-chip monitor strategy can strongly improve the calibration and control of the OPA in term of both computation time and external instruments. A typical alignment strategy in terms of pseudo-code is outlined in Fig. 10 and here we give more in-depth description of the same.

First step in calibration is the alignment of phase shifters for maximum power at the corresponding M:1 MMI type B photodetector using the, preferably, DSGD algorithm (*run_DSGD* in pseudo-code). In case there are multiple M:1 MMIs they can be optimized in parallel, each with its corresponding detector (*parfor* in pseudo-code). This allows for “divide and conquer” capability leading to further increase in speed. Once powers are maximized, we know that the phases at the input of the MMI (or end of the emitter grating) correspond to the phases that result with maximum coupling to the photodetector. These phases can be determined analytically, simulated numerically (see Fig. 9) or extracted with test structures. This is our “known phase relationship” condition between the emitters.

Second step in calibration is the extraction of the individual phase shifter efficiencies (*sweep_Phaseshifter* in pseudo-code). This step can also be parallelized between different M:1 MMIs. Keeping the rest of the phase shifters at position that results with maximum power at type B photodetector, we sweep individual phase shifters through all the available states (or sub-set of states for increased speed) recoding the modulation of the power at type B photodetector. From this response we can extract both the phase shifter efficiency (drive signal needed for 2π phase shift) as well as linearity and account for process variation as well as external influences and aging with subsequent calibrations.

Final step in calibration is the alignment of neighboring M:1 MMIs (*align_MMI* in pseudo-code) by using one of the outputs from two neighboring 1:3 MMIs and tuning the *M* phase shifters in sync like it was one grating emitter using previous calibration steps and the scattering matrices of the 1:3 and 2:1 MMIs. Once again, they can be analytically calculated, numerical simulated or extracted with test structures. The strategy for alignment between different groups of *M* gratings is very similar to the one employed in [15] where single phase shifter was tuned. At the end, we arrive to a state where we know relative phases between all the emitters as well as their efficiencies and linearities. This allows for precise control of the OPA.

The control of tuning, once system is calibrated, is relatively straightforward (*tune_Phaseshifter* in pseudo-code). The required phase shifts for given beam direction are straightforward to calculate from the emitter spacing (known by design). Control signals corresponding to these phase shifts at the grating are also straightforward to calculate from "known phase relationship" condition, MMI scattering matrices and extracted phase shifter efficiencies and linearities in the calibration step. Said functionality can be provided by e.g. microcontroller, FPGA, ASIC or PC.

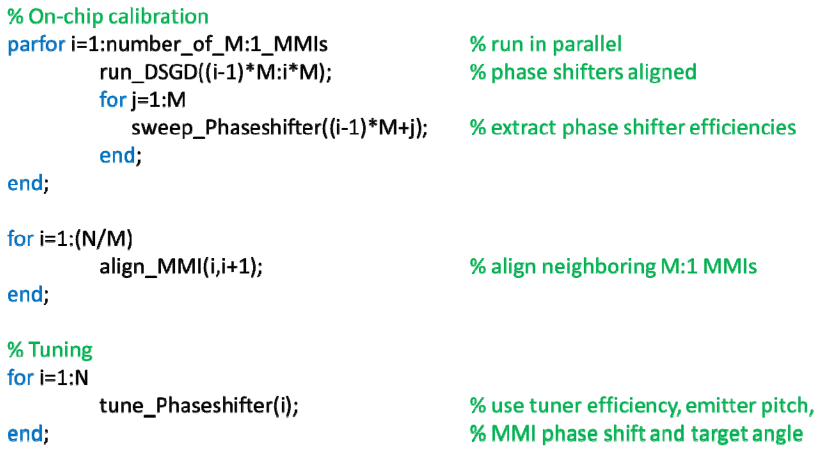

```
% On-chip calibration
parfor i=1:number_of_M:1_MMIs                  % run in parallel
          run_DSGD((i-1)*M:i*M);               % phase shifters aligned
          for j=1:M
              sweep_Phaseshifter((i-1)*M+j);   % extract phase shifter efficiencies
          end;
end;

for i=1:(N/M)
          align_MMI(i,i+1);                    % align neighboring M:1 MMIs
end;

% Tuning
for i=1:N
          tune_Phaseshifter(i);                % use tuner efficiency, emitter pitch,
end;                                           % MMI phase shift and target angle
```

Fig. 10. Pseudo-code for on-chip calibration and tuning. For details see text.

4. Conclusions

As the complexity of photonic integrated circuits (PICs) increases, control becomes more challenging. Optical phased arrays (OPA) are one of the most complex PICs with demonstrations of up to few thousands of elements with tendency for further increases in component counts. Control of such systems can be very challenging, and typically extensive calibration using external instruments is needed. Such a process is not easily scalable and also has limited usability if OPAs are deployed in commercial systems due to external influences and aging of components. An ideal OPA would have the capability to recalibrate and control itself as soon as some external condition (temperature change, time period without calibration, etc.) is reached. We proposed and analyzed such a method.

Compared to previous demonstrations, our method has significantly reduced chip footprint owning to the fact that we are using multi-mode interference (MMI) with large channel count to calibrate the system leading to significantly reduced MMI coupler lengths. The novel architecture, combined with a new optimization algorithm – deterministic stochastic gradient descent (DSGD), divide and conquer approach (parallel optimization of groups of M waveguides), and high speed modulators and detectors allows on-chip OPA calibration in ms timescales compared to many hours or days needed if standard camera based far-field optimization is pursued.

On-chip calibration and control, as outlined in this work, can pave the way for OPAs to be used in automotive, military or space industries where performance has to be guaranteed across very large temperature ranges.

Funding

Defense Advanced Research Projects Agency (DARPA) MTO (MOABB HR0011-16-C-0106).

Acknowledgments

The authors thank John Bowers from University of California, Santa Barbara and Paul Suni and James R. Colosimo from Lockheed Martin for useful discussions and encouragement. This research was developed with funding from the Defense Advanced Research Projects Agency (DARPA). The views, opinions and/or findings expressed are those of the author and should not be interpreted as representing the official views or policies of the Department of Defense or the U.S. Government.